



Titre: CT-FEM of the human thorax: Frequency response function and 3D harmonic analysis at resonance

Auteurs: Arife Uzundurukan, Sébastien Poncet, Daria Camilla Boffito, & Philippe Micheau

Date: 2024

Type: Article de revue / Article

Référence: Uzundurukan, A., Poncet, S., Boffito, D. C., & Micheau, P. (2024). CT-FEM of the human thorax: Frequency response function and 3D harmonic analysis at resonance. *Computer Methods and Programs in Biomedicine*, 246, 108062 (14 pages). <https://doi.org/10.1016/j.cmpb.2024.108062>

 **Document en libre accès dans PolyPublie**
Open Access document in PolyPublie

URL de PolyPublie: <https://publications.polymtl.ca/57579/>
PolyPublie URL:

Version: Version officielle de l'éditeur / Published version
Révisé par les pairs / Refereed

Conditions d'utilisation: CC BY
Terms of Use:

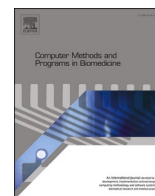
 **Document publié chez l'éditeur officiel**
Document issued by the official publisher

Titre de la revue: Computer Methods and Programs in Biomedicine (vol. 246)
Journal Title:

Maison d'édition: Elsevier BV
Publisher:

URL officiel: <https://doi.org/10.1016/j.cmpb.2024.108062>
Official URL:

Mention légale: Crown Copyright © 2024 Published by Elsevier B.V. This is an open access article under the CC BY license (<http://creativecommons.org/licenses/by/4.0/>)
Legal notice:



CT-FEM of the human thorax: Frequency response function and 3D harmonic analysis at resonance

Arife Uzundurukan^{a,*}, Sébastien Poncet^a, Daria Camilla Boffito^b, Philippe Micheau^a

^a Centre de Recherche Acoustique-Signal-Humain, Université de Sherbrooke, 2500 Bd de l'Université, Sherbrooke, QC J1K 2R1, Canada

^b Department of Chemical Engineering, École Polytechnique de Montréal, 2500 Chem. de Polytechnique, Montréal, QC H3T 1J4, Canada

ARTICLE INFO

Keywords:

Frequency response function
Computed tomography-based finite element model
Human thorax
Respiratory therapy
Resonance frequency

ABSTRACT

Background and Objective: High-frequency chest wall compression (HFCC) therapy by airway clearance devices (ACDs) acts on the rheological properties of bronchial mucus to assist in clearing pulmonary secretions. Investigating low-frequency vibrations on the human thorax through numerical simulations is critical to ensure consistency and repeatability of studies by reducing extreme variability in body measurements across individuals. This study aims to present the numerical investigation of the harmonic acoustic excitation of ACDs on the human chest as a gentle and effective HFCC therapy.

Methods: Four software programs were sequentially used to visualize medical images, decrease the number of surfaces, generate and repair meshes, and conduct numerical analysis, respectively. The developed methodology supplied the validation of the effect of HFCC through computed tomography-based finite element analysis (CT-FEM) of a human thorax. To illustrate the vibroacoustic characteristics of the HFCC therapy device, a 146-decibel sound pressure level (dB_{SPL}) was applied on the back-chest surface of the model. Frequency response function (FRF) across 5–100 Hz was analyzed to characterize the behaviour of the human thorax with the state-space model.

Results: We discovered that FRF pertaining to acceleration equals 0.138 m/s²/N at the peak frequency of 28 Hz, which is consistent with two independent experimental airway clearance studies reported in the literature. The state-space model assessed two apparent resonance frequencies at 28 Hz and 41 Hz for the human thorax. The total displacement, kinetic energy density, and elastic strain energy density were furthermore quantified at 1 μm, 5.2 μJ/m³, and 140.7 μJ/m³, respectively, at the resonance frequency. In order to deepen our understanding of the impact on internal organs, the model underwent simulations in both the time domain and frequency domain for a comprehensive analysis.

Conclusion: Overall, the present study enabled determining and validating FRF of the human thorax to roll out the inconsistencies, contributing to the health of individuals with investigating gentle but effective HFCC therapy conditions with ACDs. This innovative finding furthermore provides greater clarity and a tangible understanding of the subject by simulating the responses of CT-FEM of the human thorax and internal organs at resonance.

1. Introduction

Technological advancements in medicine have placed the Internet of Medical Devices (IoMD) in high demand in the intelligent health surveillance and rehabilitation of respiratory patients [1,2]. As a result, rehabilitation with airway clearance devices (ACDs) has shown a tendency to be independent of physiotherapists, thereby allowing patients access to treatment without any dependency on time, location, and physiotherapist availability [3]. In keeping with the above, high-frequency chest compression (HFCC) therapy using these ACDs is

deemed more practical and effective than conventional therapies with a physiotherapist [4]. While some authors conclude that there is no significant difference between ACD-based therapy and conventional physiotherapy [5], others, on the other hand, report that ACDs provide 1.8-fold higher mucus clearance per therapy session than conventional chest physical therapy [6]. Hence, the higher the demand for ACDs, the more improvements and varieties are observed in commercial devices used in aiding in the drainage of bronchial mucus and the progression of pulmonary function [7].

Given that experimental studies are limited with regard to performing a detailed investigation of inner organs in a living patient in

* Corresponding author.

E-mail address: arife.uzundurukan@usherbrooke.ca (A. Uzundurukan).

<https://doi.org/10.1016/j.cmpb.2024.108062>

Received 30 November 2023; Received in revised form 30 January 2024; Accepted 5 February 2024

Available online 9 February 2024

0169-2607/Crown Copyright © 2024 Published by Elsevier B.V. This is an open access article under the CC BY license (<http://creativecommons.org/licenses/by/4.0/>).

Nomenclature	
a	rate of introduction of gas volume per unit volume (s^{-1})
c	wave speed ($m.s^{-1}$)
E	Young's Modulus (Pa)
f	frequency (Hz)
F	external inputs of force per unit volume ($N.m^{-3}$)
K	bulk modulus (Pa.s)
k	wave number
n	time variable
u	steady-state dynamic oscillatory displacement (m)
P	dynamic pressure (Pa)
R	lung parenchyma parameters with respect to the air within
r	pore radius (m)
<i>Greek Letters</i>	
α, β	lung parenchyma parameters with respect to the air within
η	dynamic air viscosity (Pa.s)
κ	permeability (m^2)
λ	Lamé's parameter (Pa)
μ	shear modulus (Pa.s)
ν	Poisson's ratio
ρ	density ($kg.m^{-3}$)
τ	tortuosity
Φ	air volume fraction
ω	angular velocity ($m.s^{-1}$)
<i>Subscript</i>	
a	air
f	fluid
i	input
l	lungs
o	osseous region
p	porous medium
pf	fast compression
ps	slow compression
s	shear
ss	state-space
st	solid skeleton
ACD	airway clearance device
BMI	body mass index
CT	computed tomography
DICOM	digital imaging and communications in medicine
FEM	finite element modelling
FRF	frequency response function
HFCC	high frequency chest compression
IoMD	internet of medical devices
L	lungs
MRE	magnetic resonance elastography
MRI	magnetic resonance imaging
PET	positron emission tomography
O	osseous region
S	soft tissue
STL	standard triangle language
T	trachea

terms of medical ethics, numerical studies allow overcoming this limitation and promote the comprehensive investigation into inner organs in a safe and expeditious manner [8]. Two of the most essential components of accurate modelling are the implementation of geometry and the determination of material properties. Both of these elements are critical for achieving accurate results in three-dimensional finite element analysis (3D FEM) derived from computed tomography (CT) data. In addition to the accuracy of the material properties of the respiratory systems, a well-defined CT geometry plays a vital role [9]. While the importance of numerical studies is unequivocal, developing a complete and relief model for airway clearance is a relatively complex and multidisciplinary challenge as it encompasses the entire respiratory system. Furthermore, these studies explore the detailed relationship between input and output in the human thorax system through the frequency response function (FRF). They also examine various tools for feedback system analysis and design, primarily using state-space models. Accordingly, computed tomography-based finite element model (CT-FEM) has provided clinicians with useful data pertaining to inner organs such as the lungs, and particularly the bronchioles, which is crucial for the numerical illustration of the vibroacoustic effect of ACDs on the human body.

It has been common practice in modern medicine to use multi-modal clinical information from CT 3D reconstruction for medical diagnosis as well as for investigation of the impact of heavy damage on the human body in motor vehicle crash tests [10,11]. Notwithstanding, in order to optimize the potential of realistic geometry, clinical image processing has been accelerated to generate a digital twin for accurate results in 3D analysis in biomedical engineering. Medical imaging creates a visual representation of the internal organs of the body for image-guided biomedical applications such as 3D printing, analysis, diagnosis, and medical treatments [12]. It consists of magnetic resonance imaging (MRI), CT, ultrasound, positron emission tomography (PET), X-rays, etc., which are processed into the standard digital imaging and communications in medicine (DICOM) file format [13]. Various biomedical

software have been used in the literature to create a digital twin with the most popular packages being Mimics and Slicer 3D [14,15].

The determination of complex material properties plays a crucial role in FEM to obtain an accurate understanding of the problem to be solved. Human soft tissue, rib cage, and scapula are considered as viscoelastic materials and, thus, the Voigt model has been applied in order to determine their material properties [16]. Due to the material behavior of the lungs as a poroviscoelastic material, the effective medium theory and the Biot's theory have been used to investigate the physical properties of the lungs in the literature [17]. While the effective medium theory has been considered for the modelling of the lungs in acoustic studies since the 1980s [18], the latter is not valid for frequencies below 100 Hz and is only functional for the calculation of compression wave behavior [17]. Inasmuch, Biot's theory is generally preferred for yielding more accurate, reliable, and robust results over a wider frequency range and for the calculation of both compression and shear wave behaviors [13,17,23].

Low-frequency therapy is one of the applicable means to facilitate expectoration by reducing mucus viscosity. Chest resonance frequency is contingent on a multitude of factors such as body mass index (BMI), the subject's mass, height, chest size, age, and sex [20,21]. In 1994, Goodwin [21] measured the average resonance frequency of the chest wall on application of a range of frequencies between 0–100 Hz in 15 fully healthy subjects, yielding values of 25 Hz and 33 Hz for the male and female volunteers, respectively. In 2006, Ong and Ghista [20] found chest resonance frequencies of 26.7 Hz and 27.8 Hz in a sample of 23 healthy male and female volunteers, respectively. In both investigations, FRF pertaining to acceleration, alternatively referred to as inertance, exhibits prominent peaks within the range of 0.12 to 0.18 m/s^2N . In addition to the investigated low-resonance frequencies in these studies, McKusick [22] had previously reported resonance frequencies of 125 Hz, 150–175 Hz, and 300–400 Hz in men, women, and children, respectively, in 1958. As for the commercial devices investigated in the

literature, different frequencies have been used, including 15–50 Hz [20], 20–60 Hz [23], 6–19 Hz [24], 10–28.5 Hz [25], and 20 Hz [26,27]. Therefore, simulating and analyzing dynamic systems of the thorax with state-space models is instrumental in rolling out the conflation by finding the modes in the working frequency range of the ACDs. In addition to the above discrepancies, the limitations of pulmonary CT-FEM studies due to the intricate geometry and poroviscoelastic material properties of the lungs has resulted in research being predominantly focused on the computed lung model [28,29], phantom lung [30], CT image of lungs [31], and CT-based trachea [32]. With regard to ballistic and road traffic accident studies, CT-FEM human thorax models are preferentially utilized [10,11], although these models do not incorporate the complex properties of the lungs, such as the poroviscoelastic material features and air within the lungs, and moreover cannot be simulated.

In light of the latter, and given that little is known regarding the human thorax FRF along with its conflicting data, we hypothesized that an advanced and validated realistic 3D human thorax CT-FEM could address the discrepancies reported in ACDs by validating and enhancing our understanding of the thoracic response. The novelty of the present work lies in the development and validation of 3D CT-FEM for studying vibroacoustic HFCC therapy in the low-frequency range. To the best of the authors' knowledge, the model, encompassing soft tissues, bone structure, lungs, trachea, and up to approximately the fourth generation of bronchi, is the most comprehensive to date. Furthermore, the resonance frequency has been determined and confirmed in two different sets of experimental data, representing a significant contribution to a more precise determination of the operating frequency of vibroacoustic HFCC therapy devices used for treating chronic respiratory diseases. Finally, the thoracic behavior under HFCC therapy at resonance is investigated for the first time through advanced 3D simulations. In the process of creating this advanced CT-FEM, three different software programs were simultaneously utilized prior to the analysis software. For the complex material features of the lungs, Biot's theory was used in order to integrate the air properties and porous viscoelastic properties for 20 cm H₂O, whereas the Voigt theory was applied to the other

internal organs. The model was also tested state-space model at a low-frequency range of 5–100 Hz, and the time-dependent simulation was performed in COMSOL 6.1 Multiphysics. Lastly, the total displacement, kinetic energy density, and elastic strain energy density of the whole thorax were also investigated in 3D at its resonance frequency in order to gain a better understanding of the impact of acoustic excitation on internal organs.

2. Methods

2.1. CT-based medical image rendering and 3D modelling

A digital 3D realistic human thorax twin comprising the bronchial tree, lungs, soft tissue, and rib cage was developed using CT data as shown in Fig. 1. For the specific tasks of segmentation, surface reduction, surface mesh generation, and analysis, four different software packages were used to allow better supervision within each development and ultimately achieve an accurate and realistic CT-FEM.

Firstly, 3D Slicer (v5.4.0) was used during the segmentation, and the "Segment Editor Extra Effects" extension was adjusted to image an ideal range for a healthy adult male [33], with a height, weight, and chest size of 182 cm, 71.8 kg, and 101.9 cm, respectively. The DICOM file acquired for the subject through CT imaging was retrieved from the software library. Fully manual, semi-automatic, and refinement tools were furthermore used to create the entire geometry, and a thresholding range was applied to determine the region of interest and optimal Hounsfield unit values. The image of each internal organ was carefully verified and the gaps inside the segmented organs were filled completely in order to generate a smooth geometry. Generally, the high-performance finite element pre-processor HyperMesh is typically used in the literature [34,35]; however, in order to achieve the optimal intervention in each step, the following two different software were used to reduce the surface element number, generate the surface meshes, and transform the images into solid geometry prior to applying the analysis software as described below.

Secondly, in addition to its original function in bioprinting, the

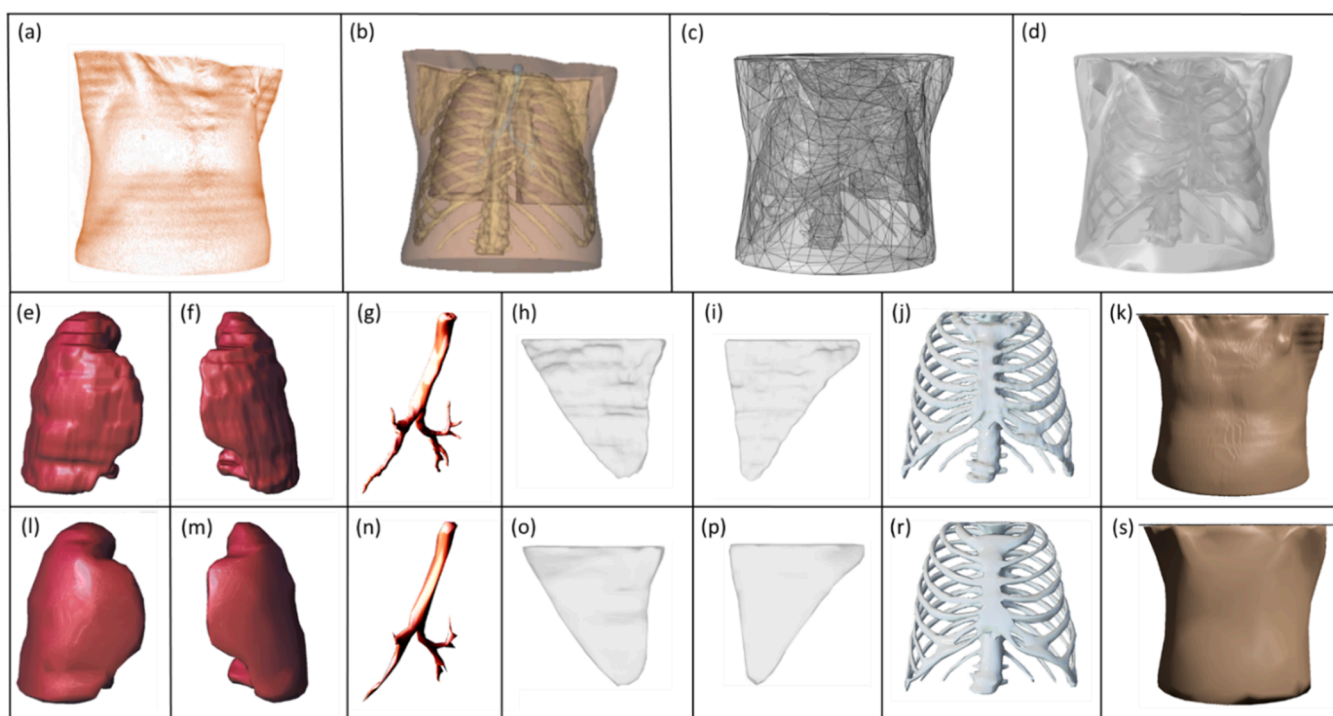


Fig. 1. Imaging, segmentation, surface meshes and simplified geometry of the CT-FEM thorax (a-d) and after the surface reduction of the right lung (e,l), left lung (f, m), trachea (g,n), right scapula (h,o), left scapula (i,p), rib cage (j,r), and soft tissues (k,s).

Meshmixer (v3.5) program was used for standard triangle language (STL) manipulation [35,36]. This software reduces the number of surface elements multiple times to generate a solid bridge for the third software, as illustrated in Fig. 1(e–s). It represents one of the intricate components of the generation of meshes in the analysis software.

Thereafter, the object's surface and triangular meshes were created for all of the individual geometries and solid asymmetries in FreeCAD (0.21.0) for the reduced surfaces as illustrated in Fig. 1(c). The assembled thorax geometry consisted of 763k elements. After a comprehensive analysis, a readable thorax model consisting of high-resolution triangle meshes for COMSOL 6.1 Multiphysics® was generated. While FreeCAD exhibits high potential for FEM in biomedical research [37], our decision was based on the critical requirement of integrating the human thorax across multiple domains with varying physics. To achieve optimal accuracy in the field of computational modeling, it is imperative to examine multiple results to ensure that the yielded data are accurate and independent of the mesh.

2.2. Material properties of the CT-FEM

The assumption is made that the soft tissue includes muscle, fat, etc., and the osseous region consists of the rib cage, scapula, sternum, etc., which are considered as viscoelastic material [19]. Therefore, the calculated material properties according to the Voigt model for both the soft tissue and osseous region were selected as summarized in Table 1.

The lungs, consisting of a unique and multi-phase porous structure, are considered as a poroviscoelastic material, while the soft tissue and osseous region are regarded as a viscoelastic material. Biot's theory for human lungs and the Voigt model for soft tissue and osseous region are used to transform the microscopic heterogeneous features of the internal organs to macroscopic homogenized features of both regions for FEM [17,42]. Biot's theory provides a more robust and accurate model than the effective medium theory for wave propagation in the lungs in terms of investigation of wave behavior under low-frequency [17,19]. As for the lungs, which is a poroviscoelastic, fully saturated, active and dynamic organ, the material's physical properties are unstable. Thus, the lungs are assumed at 20 cm H₂O, which is the appropriate pressure recommendation in low compliance between 10 and 30 cm H₂O [43,44]. For this reason, the slow wave speed (c_{sp}), fast compression wave speed (c_{pf}), and shear wave speed (c_s) were calculated according to Biot's

Table 1
Material properties used in CT-FEM for the internal organs.

List	Properties	Value	Ref.
Lungs	Air volume fraction, Φ	0.71	[17]
	Air pressure, P_a	1.03×10^5 Pa	[17]
	Air density, ρ_f	1.2 kg.m^{-3}	[17]
	Solid bulk modulus, K_t	2.2×10^9 Pa	[39]
	Solid density, ρ_t	1000 kg.m^{-3}	[39]
	Pore radius, r	0.225 mm	[40]
	Tortuosity, τ	1.33	[41]
	Permeability of porous medium, κ_p	$25.32 \times 10^{-12} \text{ m}^2$	[17]
	Dynamic air viscosity, η_f	$1.82 \times 10^{-5} \text{ Pa.s}$	[17]
	Solid skeleton bulk modulus, K_{st}	8.26×10^3 Pa	[17]
Airways	Solid shear modulus, μ_s	$1400 + 5.78(j\omega)^{0.5}$	[17]
	Young's modulus – Real part, E_1	0.28 MPa	[19]
	Young's modulus – Complex part, E_2	0.124 MPa	[19]
	Density, ρ_a	1000 kg.m^{-3}	[19]
Soft Tissue	Poisson's Ratio, ν_a	0.49998	[19]
	Lamé parameter – Real part, λ_1	2.6 GPa	[39]
	Lamé parameter – Complex part, λ_2	0	[39]
	Shear Modulus – Real part, μ_1	2.5 kPa	[39]
	Shear Modulus – Complex part, μ_2	5 Pa.s	[39]
Osseous	Density, ρ_s	1000 kg.m^{-3}	[39]
	Lamé parameter – Real part, λ_1	2.6 GPa	[39]
	Lamé parameter – Complex part, λ_2	0	[39]
	Shear modulus – Real part, μ_1	10×10^6 MPa	[39]
	Shear modulus – Complex part, μ_2	20 Pa.s	[39]
	Density, ρ_o	1500 kg.m^{-3}	[39]

theory by using the material properties for 20 cm H₂O as depicted in Table 1 using the following equations [45]:

$$\mu u_{i,jj} + \left(K_{st} + \frac{\mu}{3} \right) u_{j,ij} - (\alpha - \beta) P_i + F_i = \omega_2 (-\rho + \beta \rho_f) u_i \quad (1)$$

$$\beta P_{ii} + \Phi^2 / R \rho_f \omega^2 p + \rho_f j \omega a = -\rho_f \omega^2 (\alpha - \beta) u_{i,i} \quad (2)$$

where u is the steady-state dynamic oscillatory displacement, P represents the dynamic pressure of the air in the lungs in the frequency domain, ρ is the lung density, ρ_f represents the density of the gas in the lung, μ represents the shear viscoelasticity of the lungs, K_{st} is the bulk modulus of the solid skeleton, Φ represents the air volume fraction. F_i is the external force inputs per unit volume, ω is the angular velocity, and a is the rate of introduction of gas volume per unit volume. α , β , and R are the lung parenchyma parameters with respect to the air within [45], which are determined for 20 cm H₂O, 0.225 mm pore radius [17] and at the desired frequency value. Einstein summation notation is used in the representation of equations for simplifying the expressions by i and j index notation; elsewhere i and j represent the complex values.

$$\rho = \phi \rho_f + (1 - \phi) \rho_t \quad (3)$$

Assuming that the external excitation is negligible and there is no variation in the y and z directions, a quadratic equation is obtained using Eqs. (1) and (2). The latter provides two possible solutions; thus, the positive-valued k , which are k_{ps} and k_{pf} , are taken as the slow compression wave numbers and the fast compression wave numbers, respectively. c_{pf} and c_{ps} are calculated using the following equations:

$$c_{pf} = \omega k_{pf} \quad (4)$$

$$c_{ps} = \omega k_{ps} \quad (5)$$

Two compression waves are attenuated by the relative motion between solid and fluid by viscosity μ . As expected, the slow compression wave has a larger attenuation coefficient than the fast compression wave and the speed of the slow compression wave is more stable than that of the fast compression wave at higher frequencies [17].

For shear wave propagation, by neglecting external excitations and taking the divergence of Eq. (1) and coupling the latter with Eq. (2), where external excitation is negligible, dilatation $u_{i,i}$ is zero, as shown in Eq. (6) to illustrate shear behavior:

$$\mu u_{i,jj} = -(\rho - \beta \rho_f) \omega^2 u_i \quad (6)$$

Hence, c_s and the number of shear waves k_s are calculated by the following equations:

$$c_s = \sqrt{\frac{\mu}{\rho - \beta \rho_f}} \equiv \sqrt{\frac{\mu}{\rho}} \quad (7)$$

$$k_s = \frac{c_s}{\omega} \quad (8)$$

Therefore, c_{ps} , c_{pf} , and c_s for 20 cm H₂O are calculated for the low-frequency range, starting from 5 to 100 Hz.

2.3. Vibro-acoustic excitation modelling of the thorax

A 3D CT-FEM of the thorax was developed using COMSOL 6.1 Multiphysics® in the low-frequency domain for HFCC in an ACD setting for acoustic studies. In order to investigate the resonance frequency in the low-frequency range, ranges between 5 Hz and 100 Hz were assessed in solid mechanics in both frequency and time domains. Biot's theory has the advantage of introducing a decoupled equation for wave motion in the FEM. This method is crucial in developing a model to demonstrate the impact of acoustic excitation on the lungs with the help of acoustic ACDs.

For the purposes of this study, a 3D CT-FEM of the human thorax as a

digital twin and a cylindrical shape with a radius of 28 mm was utilized to simulate a shaker to mimic HFCC therapy. Implementing the therapy, one precisely imposed a sound pressure level of 146-decibel sound pressure level (dB_{SPL}) to designate the shaker working condition as a boundary condition of the numerical model, while intentionally keeping the other boundary conditions free as shown in Fig. 3. FRF pertaining to acceleration was obtained by selecting the cross-centered point of the cylindrical shape on the front chest wall to mimic the experimental studies in the literature. This particular point was strategically chosen for measuring acceleration in the fluctuating frequency range, minor the placement of an accelerometer on the chest wall as demonstrated in prior rigorously validated experimental studies [20,21]. This deliberate design aimed to scrutinize the impact of the shaker on the human thorax for HFCC and align the simulation more closely with real-life experimental measurement, as illustrated in Fig. 3. Moreover, the MATLAB System Identification Toolbox is employed to simulate and analyze dynamic systems of the human thorax using the 'ss' function within a state-space model, facilitating the determination of optimal fits. The resonance frequency of the thorax in the low-frequency range was then measured and compared and verified with experimental studies in the literature. After the verification of the resonance frequency, total displacement, kinetic energy density, and elastic strain energy density were subsequently investigated.

The generated surface meshes were transformed into a numerical model with 0.3 M tetrahedral elements, 54k triangles, 33k edge elements, and 5k vertex elements and solved. In addition, one of the key components of achieving this goal is through mesh independence testing, which involves determining the minimum level of mesh refinement required to obtain consistent and accurate results [38]. The errors between 0.3 M and 0.7 M cell elements for the resonance frequency and FRF were 0% and 0.3%, respectively. The drawn sensitivity resulted in different mesh grids converging at 0.3 M elements for both frequency and acceleration amplitude. The mesh grid with 0.3 M elements was hence selected for the study, in which the average element quality according to the skewness test result was 0.578.

3. Results

3.1. FRF of the human thorax and its validation

Modeling of the therapy with a shaker and an accelerometer, FRF, and phase pertaining to acceleration were illustrated in Fig. 3(a–c). FRF increased and reached the peak point at $0.138 \text{ m/s}^2\text{N}$, 28 Hz, subsequently dropping up to 60 Hz and remained relatively constant thereafter up to 100 Hz. The results indicated that the best fit with 82% accuracy is achieved with a state-space model, assessing two distinct modes with a confidence interval of 99%. The modal analysis of the

identified state-space model evaluated two apparent frequencies at 28 Hz and 41 Hz, corresponding to these two modes. For mode 1, the eigenvalues of the matrix were found to be as $-33 \pm 177i$, indicating a damping ratio of 0.19 and a natural frequency of 29 Hz. As for mode 2, it exhibited eigenvalues of $-38 \pm 270i$, with a damping ratio of 0.14 and a natural frequency of 43 Hz.

For purposes of validation, the results were compared with the mean values for female and male subjects from two different and independent experimental studies of which randomly selected samples are detailed in Table 2. As clearly observed, the numerical results of the current 3D CT-FEM were consistent with the findings of the two independent experimental studies at the frequency range of 5–100 Hz for HFCC therapy with ACDs. The first experimental study reported average chest resonance frequencies of 26.7 Hz and 27.8 Hz for male and female volunteers, respectively, while the second study showed average chest resonance frequencies of 25 Hz and 33 Hz for males and females, respectively. Moreover, sample subject number 11, which had the closest anthropometric measurements (102 cm chest size, 75 kg weight and 1.83 cm height) to our CT-FEM, also had the closest results with our numerical model.

For purposes of validation, the results were compared with the mean values for female and male subjects from two different and independent experimental studies of which randomly selected samples are detailed in Table 2. As clearly observed, the numerical results of the current 3D CT-FEM were consistent with the findings of the two independent experimental studies at the frequency range of 5–100 Hz for HFCC therapy with ACDs. The first experimental study reported average chest resonance frequencies of 26.7 Hz and 27.8 Hz for male and female volunteers, respectively, while the second study showed average chest resonance frequencies of 25 Hz and 33 Hz for males and females, respectively. Moreover, sample subject number 11, which had the closest anthropometric measurements (102 cm chest size, 75 kg weight and 1.83 cm height) to our CT-FEM, also had the closest results with our numerical model.

For acceleration results in the same direction of the excitation, y-direction, the contour plots of the analysis data depicted in Fig. 4 and Fig. 5 were limited to the validated frequency spectrum on the sternum whilst considering a wider interval of approximately $0.02 \text{ m/s}^2\text{N}$ for both the maximum and minimum values in order to better reflect the actual response. Therefore, it allows that the presented data are reliable. Furthermore, to ensure logical consistency in the results, the next capplings were determined by taking this logical consensus into consideration, in harmony with the acceleration results.

3D solutions of the acceleration at various frequencies are illustrated in Fig. 4 for 10 Hz, 20 Hz, 28 Hz, 40 Hz, and 50 Hz in panels (a,c,e,g,i), respectively. In order to gain additional information regarding internal organs in this frequency range, the 2D cross-section of the acceleration in the mid-point line of the lungs is shown at 10 Hz, 20 Hz, 28 Hz, 40 Hz, and 50 Hz in panels (b,d,f,h,j), respectively. The acceleration value onto the sternum increased for frequencies up to 28 Hz, while decreasing above this value up to 100 Hz. At 28 Hz, the lungs were under excitation with the maximum effect on the sternum, which could potentially be beneficial in draining excess mucus in HFCC therapy as also highlighted in the literature [20,21].

In order to gain a better understanding of how the waves travel in the entire thorax, various vertical cross-sections at 20 Hz, 28 Hz, and 40 Hz frequencies were considered as illustrated in Fig. 5. Cross-sections were acquired near the source of excitation (panels a,f,k), at the exact mid-line (panels b,g,l) and near (panels c,h,n) the chest surface in the xz axes, and at the mid-points of the left lung in the (x,z) plane (panels d,i,n), and mid-point of the right lung in the (y,z) plane (panels e,j,o) for 20 Hz, 28 Hz, and 40 Hz, respectively. Single pulses at 20 Hz were found to transit through each lung. However, at 28 Hz, four different crests, two in each lung, which were created near the oscillatory source, were observed travelling toward each other and eventually overlap. These superpositions producing a resultant wave with an amplitude consisting

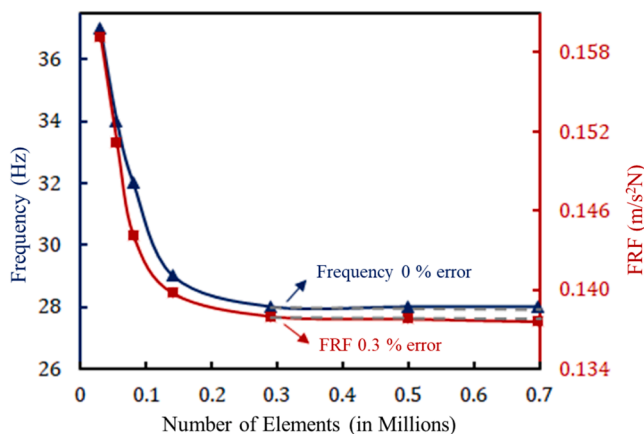


Fig. 2. Mesh independence test for frequency and FRF at resonance.

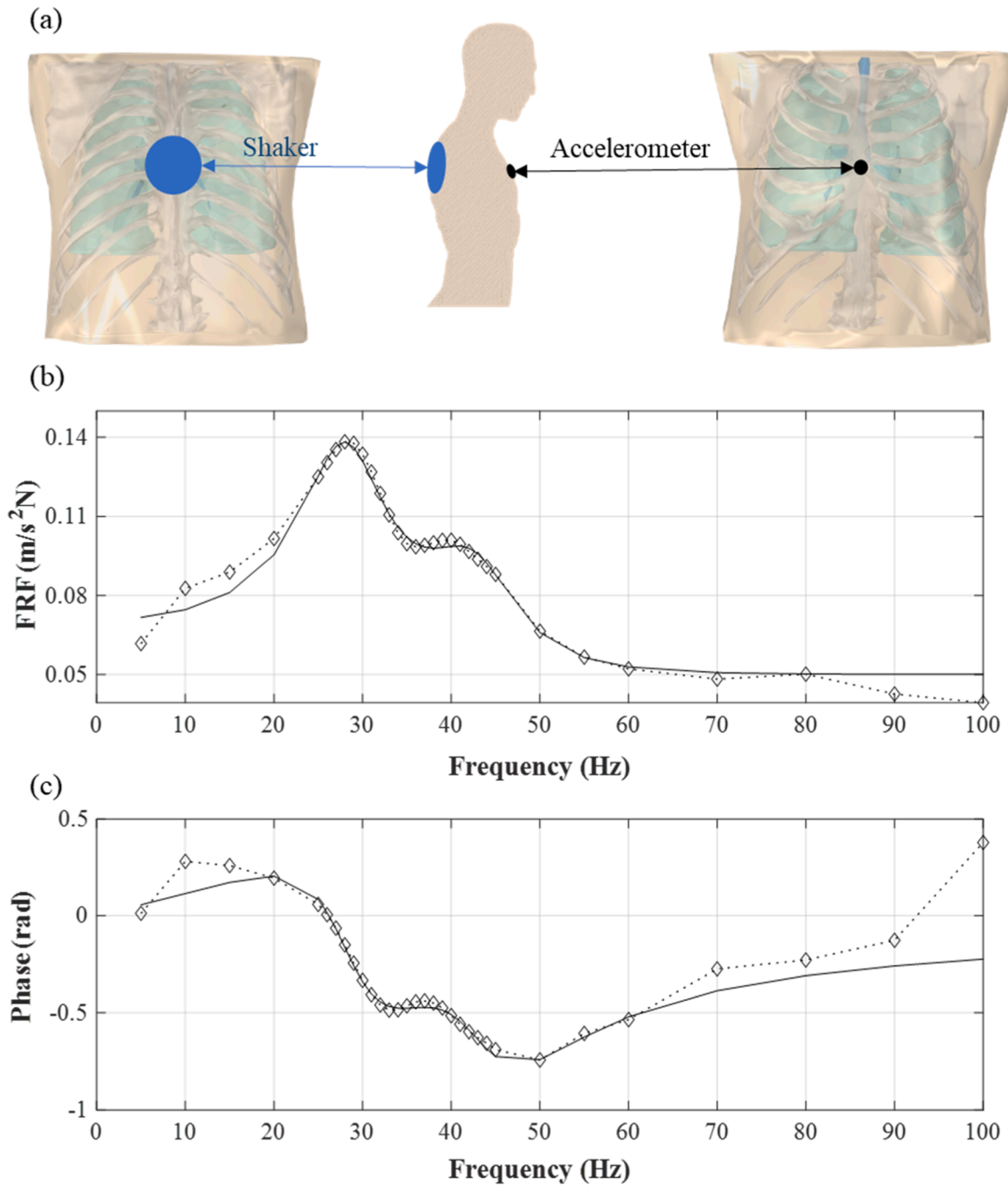


Fig. 3. (a) Modelling of the therapy, (b) FRF, and (c) phase pertaining to acceleration for an ideal healthy male thorax model.

of the sum of the individual waves occurred near the front of the chest surface.

3.2. Time-dependent simulation at resonance frequency

We next quantified the acoustic resonance frequency in time-dependent simulations by using the Inverse Fourier Transform. They were determined into the Multiphysics software in 3 different axes (x,y, z) for the displacement results at different cross-sections by using Eqs (9) to 11, respectively, where $n=(0;1;8)$. 3D CT-FEM outcomes, showcasing displacement in the y, x, and z directions and the 2D cross-sections at mid-line of the lungs both horizontally and vertically in the time domain are illustrated in Figs. 6 to 8, respectively. These visualizations correspond to different n values.

$$x(n) = \text{real}[xe^{-jn\pi/4}] \tag{9}$$

$$y(n) = \text{real}[ye^{-jn\pi/4}] \tag{10}$$

$$z(n) = \text{real}[ze^{-jn\pi/4}] \tag{11}$$

Results are plotted on the same contour plot in order to facilitate their understanding. The total displacement depicted in Fig. 9 was considered to further aid in the understanding of the analysis results. By utilizing this metric, a clear illustration of the capping points was obtained.

The observed node in the time domain displacement results were in the x-direction, showing the simultaneous reverse movement of the right and left lungs. The sternum and spinal cord aspects moved

Table 2

Comparison of the numerical results for chest resonance frequency and FRF obtained in the present study and those reported in published experimental studies in various subjects (1–13).

No	Mass (kg)	Height (cm)	Chest Size (cm)	Gender	BMI	Res. Freq. (Hz)	FRF (m/s ² N)	Ref.	
1	60	172	82	Male	20.28	28.15	For typical, 0.12–0.18, at 28 Hz, 0.13–0.14	[20]	
2	53	162	83	Male	20.2	28.35		[20]	
3	64	165	96	Male	23.51	24.43		[20]	
4	59.5	166	88.5	Male Mean	21.57	26.7		[20]	
5	48	170	69–79	Female	16.61	29.05		[20]	
6	58	164	75–86	Female	21.56	27.55		[20]	
7	51.5	161.2	73.5–83.6	Female Mean	19.85	27.81		[20]	
8	67	171	91	Female	22.9	31.3		For typical, 0.12–0.18, at 28 Hz, 0.12–0.14	[21]
9	105	185	114	Male	30.7	18.5		[21]	
10	63	178	97	Male	19.9	33.8		[21]	
11	75	183	102	Male	22.4	30		[21]	
12	80.4	178	106.1	Male	25.4	25		[21]	
13	62.4	166	89.2	Female	22.6	33		[21]	
14	71.8	182	101.9	Male	21.7	28	0.138	in this study	

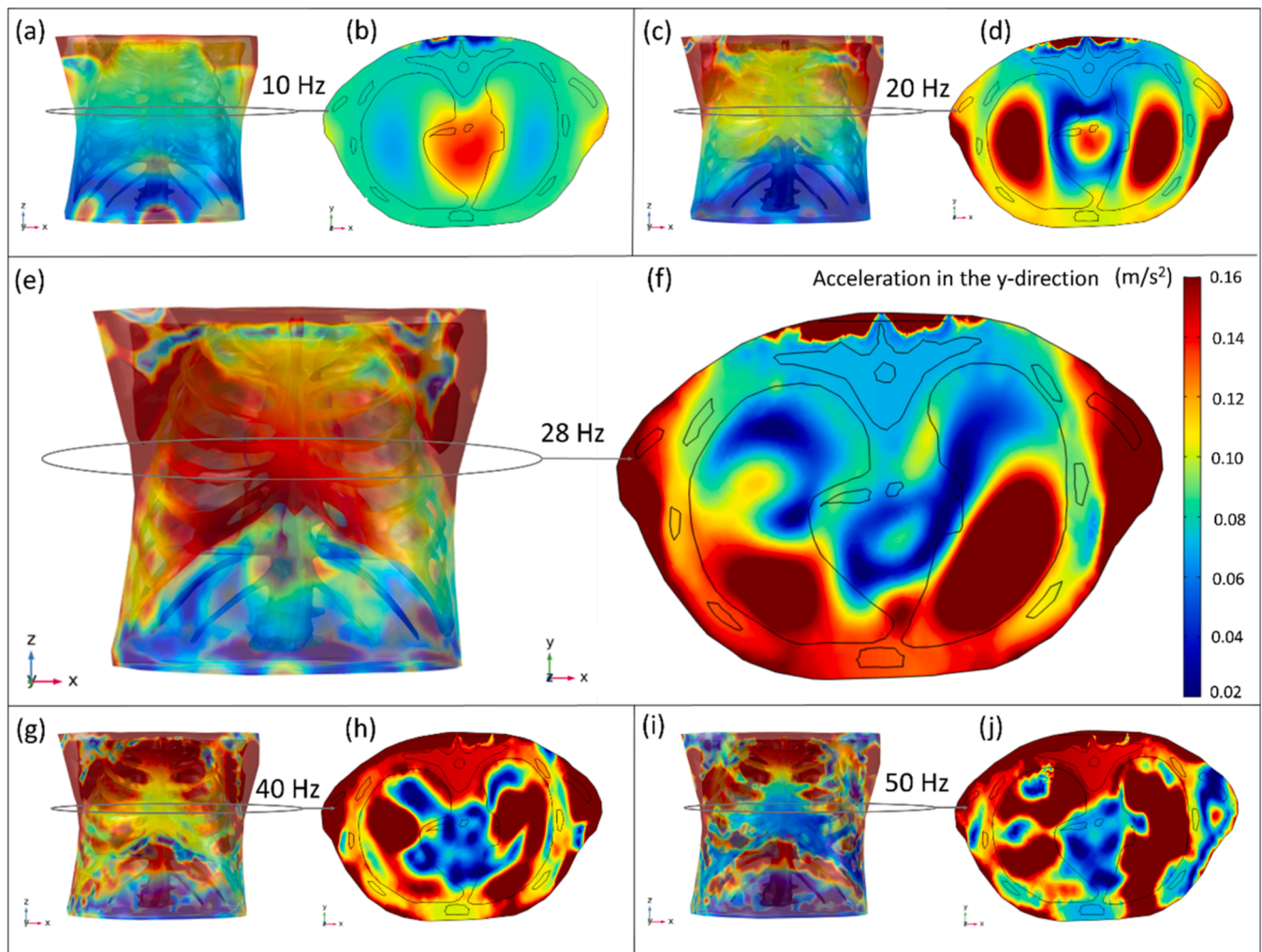


Fig. 4. Acceleration response in the y-direction of the human thorax in 3D and 2D (x,y) plane at (a,b) 10 Hz, (c,d) at 20 Hz, (e,f) at 28 Hz, (g,h) at 40 Hz, and (i,j) at 50 Hz, respectively.

independently due to their rigid and heavy physical properties compared to other internal organs in the human thorax. Furthermore, the model under the resonance frequency created by shear waves could be clearly observed in Fig. 7(e) and Fig. 7(k) whereby the left and right lungs had counterwise movements in addition to having an interwoven movement.

3.3. Displacement and energy analysis at resonance

Different solutions for total displacement depicted in Figs. 6 to 8, were further explored in addition to kinetic energy density and elastic strain energy density, shown in Fig. 9. At 28 Hz, 3D CT-FEM was in resonance, indicating that the thorax is able to store and easily transfer the energy and tends to vibrate at a higher amplitude. Variations in

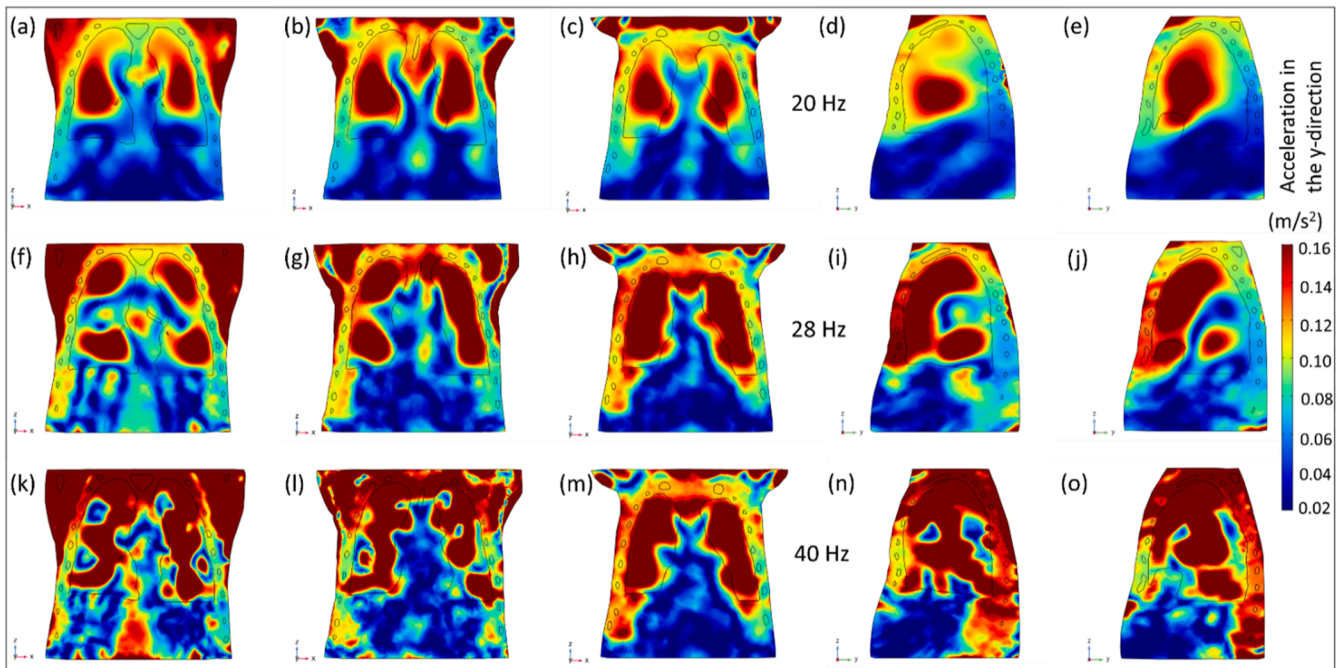


Fig. 5. Vertical cross-sections of the thorax for the acceleration response in the y-direction near the source of excitation (a,f,k); at mid-line (b,g,l) and near the chest surface (c,h,m) in the (x,z) plane; at mid-point of the left lung (d,i,n) and at mid-point of the right lung (e,j,o) in the (y,z) plane at 20 Hz, 28 Hz, and 40 Hz, respectively.

tissue material properties resulted in significant differences in energy density distribution throughout the human body. This phenomenon was exemplified by the diverse range of tissues selected, including bone and lungs. Contour plots, used to represent this distribution with respect to the maximum and minimum results, allowed for a comprehensive visualization of the data and provided a detailed examination of the distribution patterns.

3D solutions of the total displacement, kinetic energy density, and elastic strain energy density are shown at the mid-line cross sections of the lungs for both y and z axes at the resonance frequency in Fig. 9(a–c), (d–f), (g–i), respectively. The average values of total displacement, kinetic energy density, and elastic strain energy density were $1 \mu\text{m}$, $5.2 \mu\text{J}/\text{m}^3$, and $140.7 \mu\text{J}/\text{m}^3$, respectively at the resonance frequency. For the total displacement result, the highest displacement occurred in the y-direction as expected. This is in keeping with the values observed in Figs. 6 to 8 whereby the compression waves were predominant. Furthermore, the cross-section images on both vertical and horizontal aspects provide a good indication of the excitation effect on the lungs. The manner in which compression waves behaved in the lungs appeared similar to their behavior in the remainder of the body. However, such interpretation differed for the lungs when considering their cross-sectional geometries since the kinetic energy density is also dependent on the material properties in addition to the velocity of the particles. As for the elastic strain energy density, depending on the material properties and displacement formulation, it mostly accumulated in the osseous region and the trachea when taking the whole body into consideration.

4. Discussion

Despite the fact that resonance frequency is crucial for providing an effective and gentle therapy with the assistance of ACDs, there are many inconsistencies with regard to its reported values. For instance, Goodwin [21] applied a frequency range of 0–100 Hz in 15 male and female volunteers and found a resonance frequency of 25 Hz and 33 Hz. Ong and Ghista [20] conducted another study with 23 healthy male and female volunteers and found a resonance frequency of 26.7 Hz and 27.8

Hz for the chest wall in the frequency range of 18–34 Hz. These two studies are thus in agreement with each other, as they both found relatively similar resonance frequencies. However, McKusick [22] in 1958 reported quite different findings, with resonance frequencies in the range of 125 Hz, 150–175 Hz, and 300–400 Hz for men, women, and children, respectively. Moreover, there are other studies reporting resonance frequencies of 6.5 Hz [8] and 6.1 Hz [46]. The advent of numerical, 3D modelling thus represents a valuable alternative for investigating resonance frequency and its effects on internal organs in terms of providing both repeatability and reliability in this field.

In the present study, a highly advanced, validated, easily simulated and realistic 3D CT-FEM of the human thorax consisting of soft tissues, rib cage, lungs, trachea and its branches, was tested in both the frequency-domain and time-domain allowing to reveal the resonance frequency effect on the human thorax in comprehensive detail. Four different software were simultaneously used as a complementary component of the simulation. Despite the intricately complex geometry of the human thorax, the results were consistent with two different experimental data reported in the literature for both female and male samples [20,21]. Moreover, verification was conducted in different positions: at an acceleration response of 0.138 m/s^2 at 28 Hz, the superposition was observed near the front of the chest surface, which is extremely difficult to ascertain experimentally. Due to the constructive interference, the effect in the lungs near the sternum contributed greatly toward determining the chest resonance frequency. The outcomes of our study identify a state-space model with a confidence interval of 99% and an accuracy of 82%, which attests to the robustness of the model in capturing the underlying dynamics of the system. The modal analysis assessed two apparent resonance frequencies at 28 Hz and 41 Hz. These findings contribute significantly to our understanding of the system's response characteristics, providing valuable insights into its dynamic behavior. Therefore, the robust dynamics of generated human thorax model opens avenues for optimizing its performance and addressing potential challenges in various applications. Developing a poromechanical multiscale model bridges alveolar features to organ-level function by capturing how structural changes in the tissue influence mechanics [47]. Therefore, using Biot's theory for the multiscale model

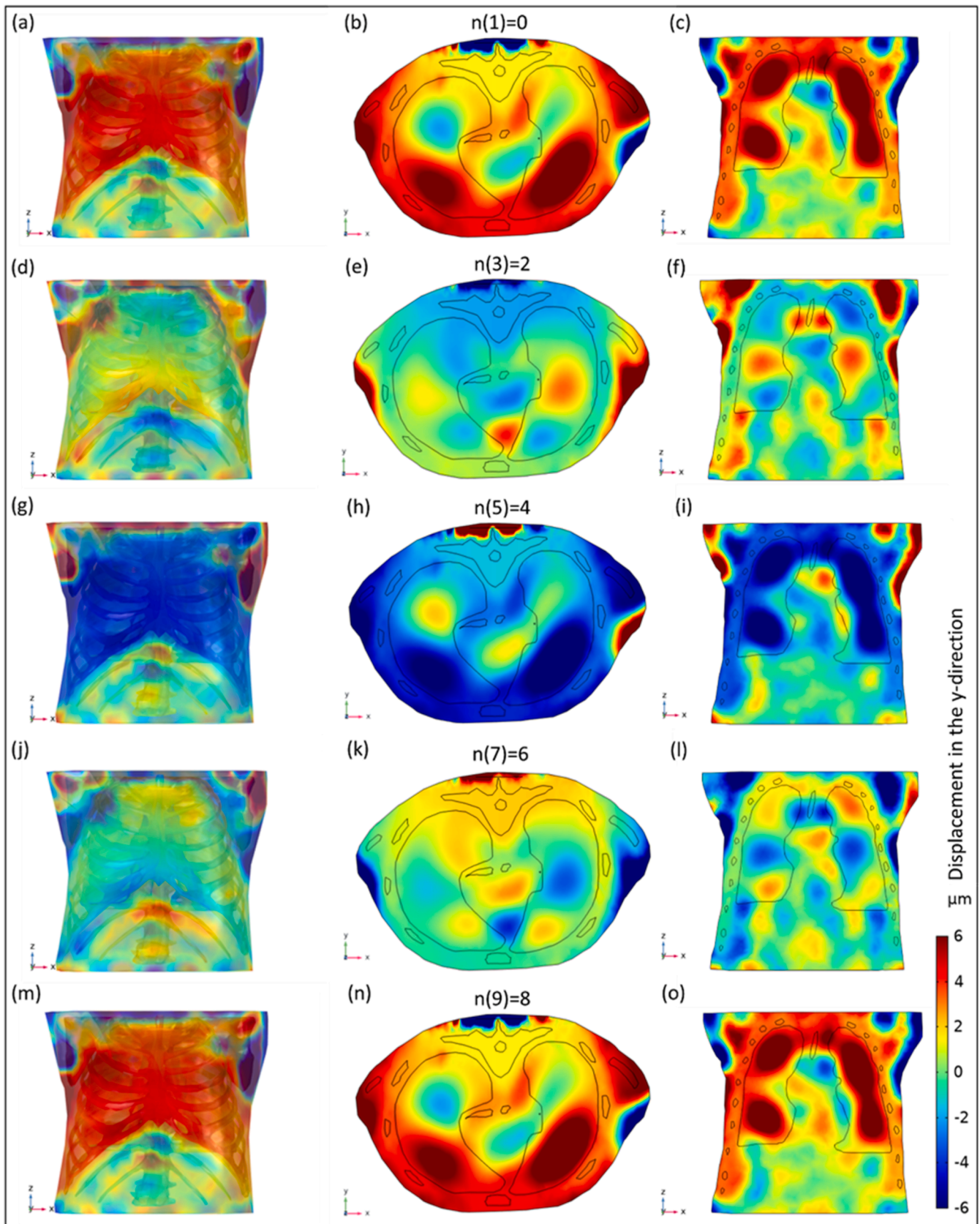


Fig. 6. Human thorax response in 3D (a,d,g,j,m), 2D (x,y) plane (b,e,h,k,n), and 2D (x,z) plane (c,f,i,l,o) of the displacement in the y-direction according to n values 0, 2, 4, 6, and 8, respectively at 28 Hz.

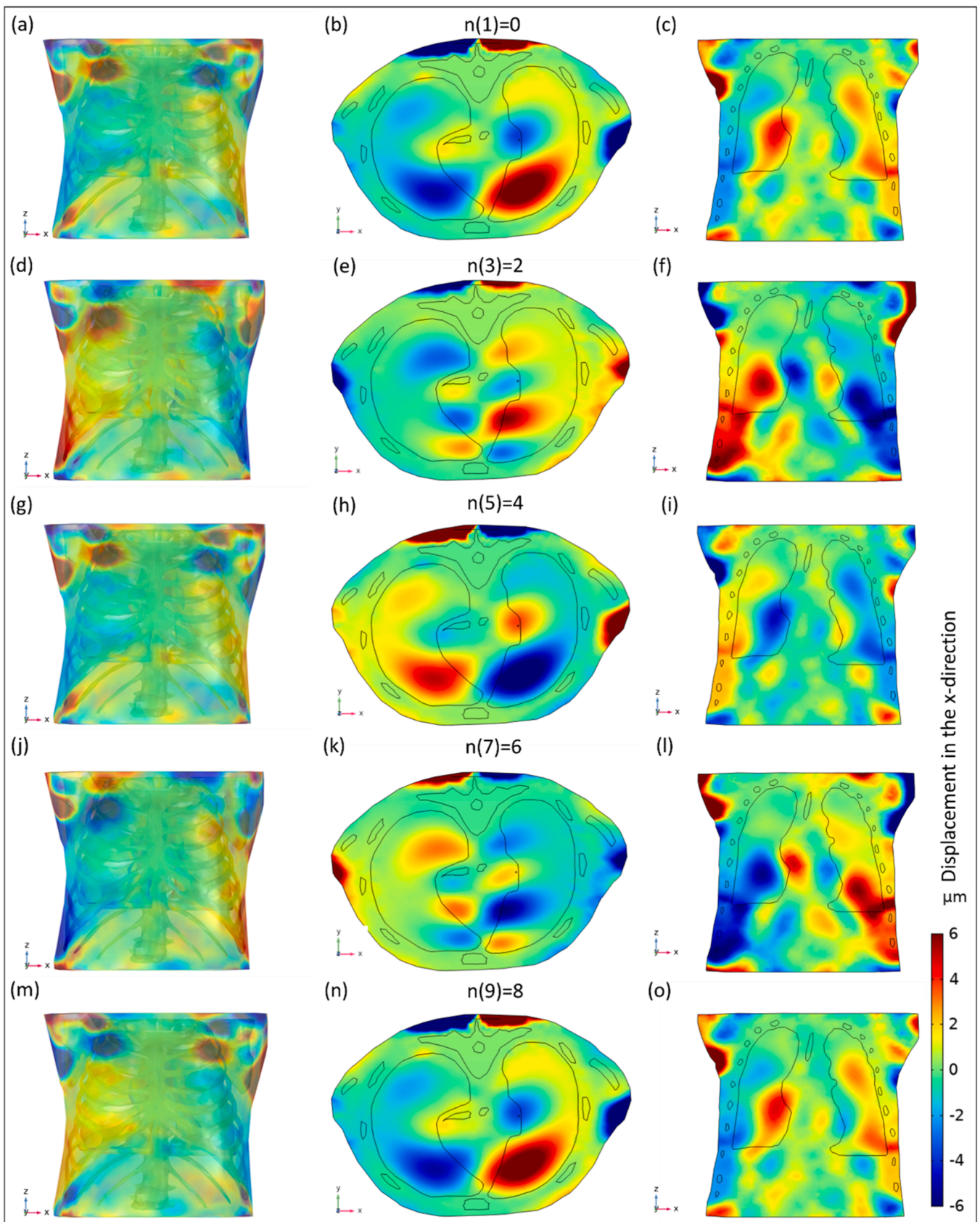


Fig. 7. Human thorax response in 3D (a,d,g,j,m), 2D (x,y) plane (b,e,h,k,n), and 2D (x,z) plane (c,f,i,l,o) of the displacement in the x-direction according to n values 0, 2, 4, 6, and 8, respectively at 28 Hz.

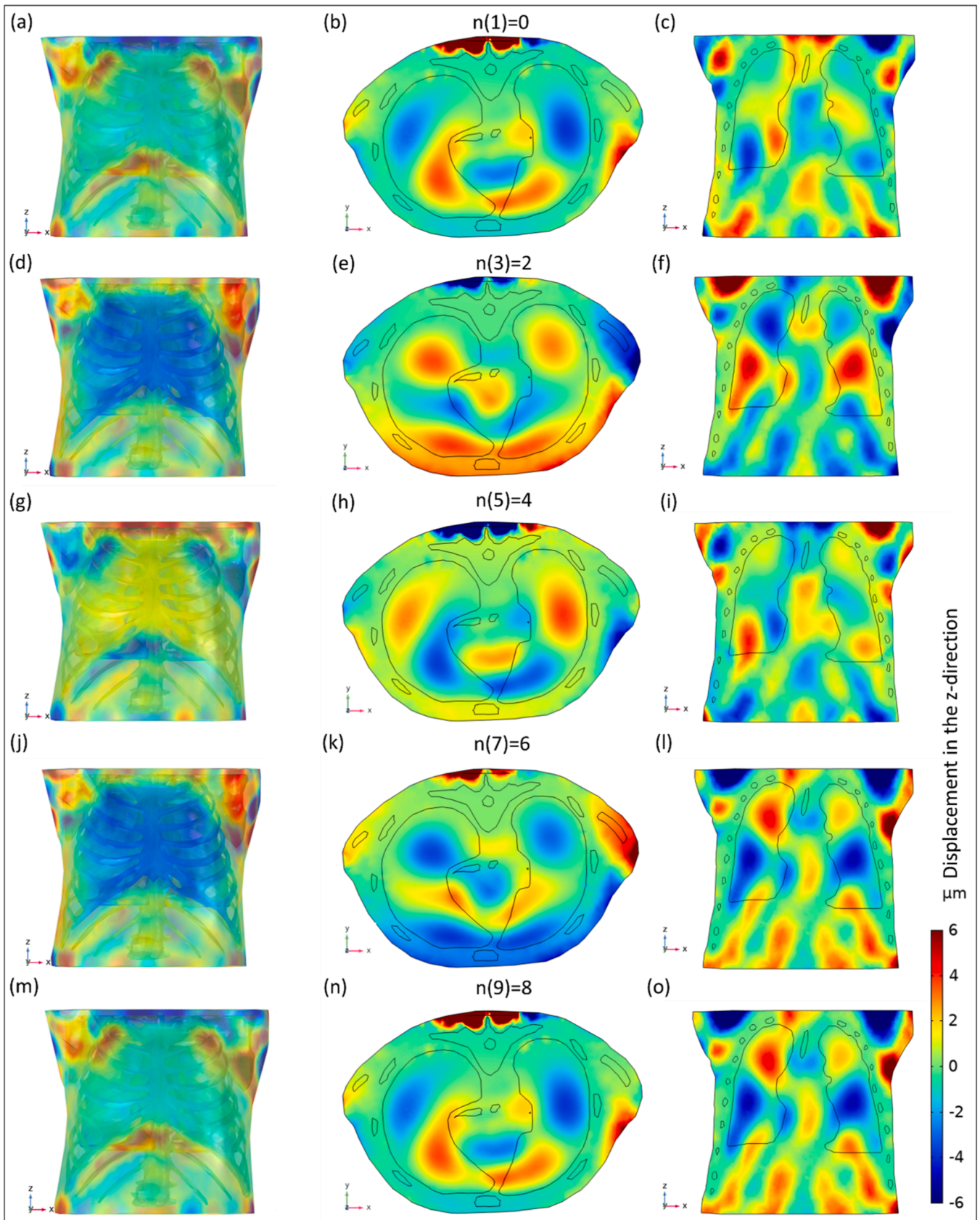


Fig. 8. Human thorax response in 3D (a,d,g,j,m), 2D (x,y) plane (b,e,h,k,n), and 2D (x,z) plane (c,f,i,l,o) of the displacement in the z-direction according to n values 0, 2, 4, 6, and 8, respectively at 28 Hz.

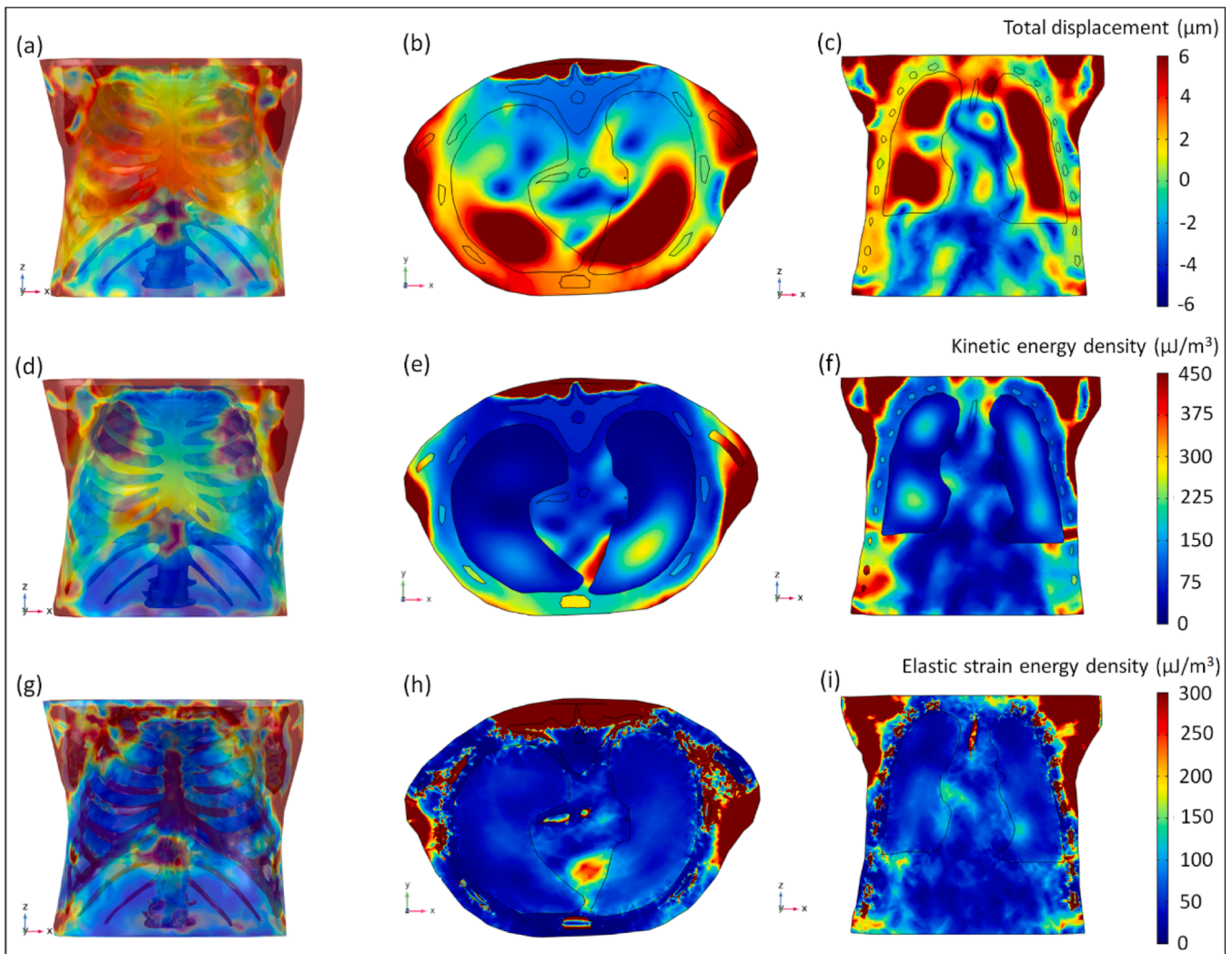


Fig. 9. Human thorax response in 3D, 2D (x,y) and (x,z) planes for total displacement (a-c), kinetic energy density (d-f), and elastic strain energy density (g-i), respectively, at the resonance frequency, 28 Hz.

helps obtain numerical results to represent alveolar features at 20 cm H₂O in this study. This approach enables a comprehensive understanding of the complex mechanics and effects of HFCC on the lungs. As for higher frequencies, in addition to constructive interference, destructive interference also occurred to lessen the sum of the individual waves. At the resonance frequency, we furthermore conducted a time-dependent analysis of the displacement results given that the attenuation of the slow compression wave occurs at a much quicker rate than the fast compression wave [19]. We were able to document the internal organs by simulation of the propagation of the displacement in different axes under acoustic excitation. As depicted in Fig. 7(e,k), the left and right lungs exhibited a counterwise movement in addition to having an interwoven movement. Simultaneous movement in various directions can create more air circulation inside the bronchi, bronchioles and air sacs. This may constitute an additional explanation for the high effectiveness of HFCC therapy observed in the experimental studies, which were introduced by numerical analysis owing to the generated realistic 3D FEM of the human thorax. Each human organ has its unique material features whereby the wave travels by attenuation and amplification from one to the other. Given that the geometry consists of intricate geometries and complex material properties, in addition to having two different methods for the simulation of shear waves in biological tissues, there are many absorptions from one material to another. When the geometry was taken into consideration, there were still emissive and

absorbing effects as a result of rib cage geometry and material properties, which constitutes a challenging surrounding material. Given the latter, the model was simulated in the time-domain in addition to the frequency-domain analysis in order to provide a better understanding of the resonance frequency effect on the internal organs. The CT-FEM simulation files in various axes are given as e-videos as a supplement to this study.

The importance of resonance frequency lies in the absorption or dissipation of the maximum amount of energy, which in turn could supply the highest vibration and maximum kinetic and potential energy with a simple pendulum. The mean values for total displacement, kinetic energy density and elastic strain energy density in the human thorax were observed at $1 \mu\text{m}$, $5.2 \mu\text{J}/\text{m}^3$, and $140.7 \mu\text{J}/\text{m}^3$, respectively at the resonance frequency. While the material properties of the inner organs were affected by the frequency, the precise impact on each organ was nonetheless complex as illustrated herein in the 3D results and simulations. Fig. 3 provides an illustration of the experimental studies' methodology and measurement method for the 3D FEM, which was validated by FRF. However, to enhance validation, magnetic resonance elastography (MRE), an advanced medical imaging technique integrated with MRI, can be utilized for the noninvasive estimation of mechanical properties in both soft tissue and osseous regions in vivo. This is particularly valuable as MRE enables a thorough examination of wavelength variations in the soft tissue and osseous regions by analyzing the

displacement of shear waves [48].

In conclusion, the present study contributes towards revealing the uncertainties of the operating frequency range of HFCC. This represents a ground-breaking advance in acoustic ACDs enabling bringing clarity to FRF. Importantly, the findings herein further contribute to the understanding of thoracic behavior during chest physiotherapy at the resonance frequency and demonstrate the value-added practical contribution of the use of CT-FEM in providing repeatability and reliability in this field. Notwithstanding, the limitation of this new, realistic, and validated 3D FEM lies in not taking into account bronchial mucus, its properties, and its transport in the lungs. As a first step in this direction, the future study will focus on the transport of mucus in bronchioles subject to deformation as identified by the present model. Therefore, the optimal working conditions of ACDs could be reflected on the rheological properties of bronchial mucus.

Statements of ethical approval

Not required.

Funding

None obtained.

Author contributions

AU conducted a literature review, performed the CT-FEM analysis, interpreted the analysis results, and drafted the manuscript. SP and PM also contributed to the literature review and provided valuable insight into the CT-FEM results. The overall idea was conceived by SP, DCB, and PM who supervised the project and provided critical feedback for manuscript revision.

CRedit authorship contribution statement

Arife Uzundurukan: Writing – review & editing, Writing – original draft, Visualization, Validation, Software, Resources, Methodology, Investigation, Formal analysis, Conceptualization. **Sébastien Poncet:** Writing – review & editing, Supervision, Software, Resources, Project administration, Methodology, Funding acquisition, Conceptualization. **Daria Camilla Boffito:** Writing – review & editing, Supervision, Resources, Project administration, Methodology, Funding acquisition, Conceptualization. **Philippe Micheau:** Writing – review & editing, Supervision, Software, Resources, Project administration, Methodology, Funding acquisition, Conceptualization.

Declaration of competing interest

The authors declare that they have no known competing financial interests or personal relationships that could have influenced the present work.

References

- [1] M.Z. Rahman, M.A. Akbar, V. Leiva, A. Tahir, M.T. Riaz, C. MartinBarreiro, An intelligent health monitoring and diagnosis system based on the internet of things and fuzzy logic for cardiac arrhythmia COVID-19 patients, *Comput. Biol. Med.* 154 (2023) 106583.
- [2] J. Zhang, J. Wu, Y. Qiu, A. Song, W. Li, X. Li, Y. Liu, Intelligent speech technologies for transcription, disease diagnosis, and medical equipment interactive control in smart hospitals: a review, *Comput. Biol. Med.* (2023) 106517.
- [3] G. Leemans, D. Belmans, C. Van Holsbeke, B. Becker, D. Vissers, K. Ides, S. Verhulst, K. Van Hoorenbeek, The effectiveness of a mobile high-frequency chest wall oscillation (HFCWO) device for airway clearance, *Pediatr. Pulmonol.* 55 (8) (2020) 1984–1992.
- [4] H. Gorby, M.C. Urribarri, When to leverage high-frequency chest wall Oscillation: a roundtable discussion with pulmonologists, *Respir. Ther.* 18 (1) (2023) 33–36.
- [5] M. Maxwell, A. Redmond, Comparative trial of manual and mechanical percussion technique with gravity-assisted bronchial drainage in patients with cystic fibrosis, *Arch. Dis. Child* 54 (7) (1979) 542–544.
- [6] L. Hansen, W. Warwick, High-frequency chest compression system to aid in clearance of mucus from the lung, *Biomed. Instrum. Technol.* 24 (4) (1990) 289–294.
- [7] J. Ge, Y. Ye, Y. Tan, F. Liu, Y. Jiang, J. Lu, High-frequency chest wall oscillation multiple times daily can better reduce the loss of pulmonary surfactant and improve lung compliance in mechanically ventilated patients, *Heart & Lung* 61 (2023) 114–119.
- [8] M. Brunengo, Study of a Visco-Elastic Model of the Human Lung and Application to the High Frequency Chest Wall oscillation, PhD Dissertation, Université Côte d'Azur, 2021.
- [9] J. Li, J. Ma, J. Dong, W. Yang, J. Tu, L. Tian, Total and regional microfiber transport characterization in a 15th-generation human respiratory airway, *Comput. Biol. Med.* 163 (2023) 107180.
- [10] D. Poulard, R.W. Kent, M. Kindig, Z. Li, D. Subit, Thoracic response targets for a computational model: a hierarchical approach to assess the biofidelity of a 50th-percentile occupant male finite element model, *J. Mech. Behav. Biomed. Mater.* 45 (2015) 45–64.
- [11] S. Roth, F. Torres, P. Feuerstein, K. Thoral-Pierre, Anthropometric dependence of the response of a thorax FE model under high speed loading: validation and real world accident replication, *Comput. Methods Programs Biomed.* 110 (2) (2013) 160–170.
- [12] H.-Y. Zhou, Y. Yu, C. Wang, S. Zhang, Y. Gao, J. Pan, J. Shao, G. Lu, K. Zhang, W. Li, A transformer-based representation-learning model with unified processing of multimodal input for clinical diagnostics, *Nat. Biomed. Eng.* 7 (2023) 743–755.
- [13] G. Wang, X. Liu, J. Shen, C. Wang, Z. Li, L. Ye, X. Wu, T. Chen, K. Wang, X. Zhang, et al., A deep-learning pipeline for the diagnosis and discrimination of viral, non-viral and COVID-19 pneumonia from chest x-ray images, *Nat. Biomed. Eng.* 5 (6) (2021) 509–521.
- [14] H. Palnitkar, B.M. Henry, Z. Dai, Y. Peng, H.A. Mansy, R.H. Sandler, R.A. Balk, T. J. Royston, Sound transmission in human thorax through airway insonification: an experimental and computational study with diagnostic applications, *Med. Biol. Eng. Comput.* 58 (10) (2020) 2239–2258.
- [15] J. Kalpathy-Cramer, J.B. Freymann, J.S. Kirby, P.E. Kinahan, F.W. Prior, Quantitative imaging network: data sharing and competitive algorithm validation leveraging the cancer imaging archive, *Transl. Oncol.* 7 (1) (2014) 147–152.
- [16] F. Dogan, M. Serdar Celebi, Real-time deformation simulation of non-linear viscoelastic soft tissues, *Simulation.* 87 (3) (2011) 179–187.
- [17] Z. Dai, Y. Peng, H.A. Mansy, R.H. Sandler, T.J. Royston, Comparison of poroviscoelastic models for sound and vibration in the lungs, *J. Vib. Acoust.* 136 (5) (2014) 1–11.
- [18] D.A. Rice, Sound speed in pulmonary parenchyma, *J. Appl. Physiol.* 54 (1) (1983) 304–308.
- [19] Z. Dai, Y. Peng, B.M. Henry, H.A. Mansy, R.H. Sandler, T.J. Royston, A comprehensive computational model of sound transmission through the porcine lung, *J. Acoust. Soc. Am.* 136 (3) (2014) 1419–1429.
- [20] J. Ong, D. Ghista, Applied chest-wall vibration therapy for patients with obstructive lung disease, *Human Respiration: Anatomy and Physiology, Mathematical Modeling, Numer. Simul. Appl.* 3 (2006) 157–167.
- [21] M. Goodwin, Measurement of resonant frequencies in the human chest, *Proceedings of the Institution of Mechanical Engineers, Part H, J. Eng. Med.* 208 (2) (1994) 83–89.
- [22] V. McKusick, Cardiovascular sound in health and disease, *JAMA* 169 (9) (1959) 1013.
- [23] D. Schieppati, R. Germon, F. Galli, M.G. Rigamonti, M. Stucchi, D.C. Boffito, Influence of frequency and amplitude on the mucus viscoelasticity of the novel mechano-acoustic Frequencer™, *Respir. Med.* 153 (2019) 52–59.
- [24] J. Kluff, L. Bekker, M. Castagnino, J. Gaiser, H. Chaney, R.J. Fink, A comparison of bronchial drainage treatments in cystic fibrosis, *Pediatr. Pulmonol.* 22 (4) (1996) 271–274.
- [25] A.P. Dos Santos, R.C. Guimaraes, E.M. de Carvalho, A.C. Gastaldi, Mechanical behaviors of Flutter VRP1, Shaker, and Acapella devices, *Respir. Care* 58 (2) (2013) 298–304.
- [26] International Biophysics Corporation, The AffloVest - The History and the Future of the HFCWO Market, 2013.
- [27] M. Brunengo, B.R. Mitchell, A. Nicolini, B. Rousselet, B. Mauroy, Optimal efficiency of high-frequency chest wall oscillations and links with resistance and compliance in a model of the lung, *Phys. Fluids* 33 (12) (2021) 121909.
- [28] A.K. Kumar, S. Jain, S. Jain, M. Ritam, Y. Xia, R. Chandra, Physics informed neural entangled-ladder network for inhalation impedance of the 38 respiratory system, *Comput. Methods Programs Biomed.* 231 (2023) 107421.
- [29] M. Sabz, R. Kamali, S. Ahmadzade, Numerical simulation of magnetic drug targeting to a tumor in the simplified model of the human lung, *Comput. Methods Programs Biomed.* 172 (2019) 11–24.
- [30] A. González-Suárez, R.M. Irastorza, S. Deane, B. O'Brien, M. O'Halloran, A. Elahi, Full torso and limited-domain computer models for epicardial pulsed electric field ablation, *Comput. Methods Programs Biomed.* 221 (2022) 106886.
- [31] X. Zhang, M. Luo, E. Wang, L. Zheng, C. Shu, Numerical simulation of magnetic nano drug targeting to atherosclerosis: effect of plaque morphology (stenosis degree and shoulder length), *Comput. Methods Programs Biomed.* 195 (2020) 105556.
- [32] H. Dang, J. Yang, L. Chen, Y. Xu, The airflow and cooling characteristics in the airway of NHBD lung with hypothermic ventilation, *Int. J. Ther. Sci.* 177 (2022) 107588.

- [33] B. Shah, K. Sucher, C.B. Hollenbeck, Comparison of ideal body weight equations and published height-weight tables with body mass index tables for healthy adults in the United States, *Nutr. Clin. Practice* 21 (3) (2006) 312–319.
- [34] W. Hua, J. Zhi, B. Wang, W. Ke, W. Sun, S. Yang, L. Li, C. Yang, Biomechanical evaluation of adjacent segment degeneration after one-or two-level anterior cervical discectomy and fusion versus cervical disc arthroplasty: a finite element analysis, *Comput. Methods Programs Biomed.* 189 (2020) 105352.
- [35] J. Kang, Y. Tian, J. Zheng, D. Lu, K. Cai, L. Wang, D. Li, Functional design and biomechanical evaluation of 3D printing peek flexible implant for chest wall reconstruction, *Comput. Methods Programs Biomed.* 225 (2022) 107105.
- [36] G.P. Carmo, M. Dymek, M. Ptak, R.J. Alves-de Sousa, F.A. Fernandes, Development, validation and a case study: the female finite element head model (FeFEHM), *Comput. Methods Programs Biomed.* 231 (2023) 107430.
- [37] G.M. Eremina, A.Y. Smolin, Risk assessment of resurfacing implant loosening and femur fracture under low-energy impacts taking into account degenerative changes in bone tissues. computer simulation, *Comput. Methods Programs Biomed.* 200 (2021) 105929.
- [38] S. Knotek, S. Schmelter, M. Olbrich, Assessment of different parameters used in mesh independence studies in two-phase slug flow simulations, *Measurement: Sensors* 18 (2021) 100317.
- [39] H.E. Von Gierke, H.L. Oestreicher, E.K. Franke, H.O. Parrack, W.W. von Wittern, Physics of vibrations in living tissues, *J. Appl. Physiol.* 4 (12) (1952) 886–900.
- [40] A.J. Hajari, D.A. Yablonskiy, A.L. Sukstanskii, J.D. Quirk, M.S. Conradi, J. C. Woods, Morphometric changes in the human pulmonary acinus during inflation, *J. Appl. Physiol.* 112 (6) (2012) 937–943.
- [41] G. Bonnet, J.-L. Auriault, Dynamics of saturated and deformable porous media: homogenization theory and determination of the solid-liquid coupling coefficients, in: *Physics of Finely Divided Matter: Proceedings of the Winter School*, Springer, Les Houches, France, 1985, pp. 306–316. March 25–April 5, 1985.
- [42] T.J. Royston, Z. Dai, R. Chaunsali, Y. Liu, Y. Peng, R.L. Magin, Estimating material viscoelastic properties based on surface wave measurements: a comparison of techniques and modeling assumptions, *J. Acoust. Soc. Am.* 130 (6) (2011) 4126–4138.
- [43] J.D. Marks, A. Schapera, R.W. Kraemer, J.A. Katz, Pressure and flow limitations of anesthesia ventilators, *Anesthesiology* 71 (3) (1989) 403–408.
- [44] L. Gattinoni, F. Collino, G. Maiolo, F. Rapetti, F. Romitti, T. Tonetti, F. Vasques, M. Quintel, Positive end-expiratory pressure: how to set it at the individual level, *Ann. Transl. Med.* 5 (14) (2017) 1–10.
- [45] M. Schanz, *Wave Propagation in Viscoelastic and Poroelastic continua: a Boundary Element Approach (Lecture Notes in Applied Mechanics)*, 3rd Edition, 2, Springer Science & Business Media, Berlin, Heidelberg, 2012.
- [46] G. Hahn, Resonant frequency of the chest-lung system by analysis of the respiratory flow curve, *Comp. Biochem. Physiol. A, Comp. Physiol.* 96 (4) (1990) 499–502.
- [47] D.E. Hurtado, N. Avilés-Rojas, F. Concha, Multiscale modeling of lung mechanics: from alveolar microstructure to pulmonary function, *J. Mech. Phys. Solids.* 179 (2023) 105364.
- [48] M. Chakouch, F. Charleux, P. Pouletaut, S. Bensamoun, MR elastography of the human lung, *State Art Bioeng.* 2 (1) (2022) 1–15.